

ReynoldsFlow: Exquisite Flow Estimation via Reynolds Transport Theorem

Yu-Hsi Chen

The University of Melbourne
Parkville, Australia

yuhsi@student.unimelb.edu.au

Chin-Tien Wu

National Yang Ming Chiao Tung University
Hsinchu City, Taiwan

ctw@math.nctu.edu.tw

Abstract

Optical flow is a fundamental technique for motion estimation, widely applied in video stabilization, interpolation, and object tracking. Recent advancements in artificial intelligence (AI) have enabled deep learning models to leverage optical flow as an important feature for motion analysis. However, traditional optical flow methods rely on restrictive assumptions, such as brightness constancy and slow motion constraints, limiting their effectiveness in complex scenes. Deep learning-based approaches require extensive training on large domain-specific datasets, making them computationally demanding. Furthermore, optical flow is typically visualized in the HSV color space, which introduces nonlinear distortions when converted to RGB and is highly sensitive to noise, degrading motion representation accuracy. These limitations inherently constrain the performance of downstream models, potentially hindering object tracking and motion analysis tasks. To address these challenges, we propose Reynolds flow, a novel training-free flow estimation inspired by the Reynolds transport theorem, offering a principled approach to modeling complex motion dynamics. Beyond the conventional HSV-based visualization, denoted ReynoldsFlow, we introduce an alternative representation, ReynoldsFlow+, designed to improve flow visualization. We evaluate ReynoldsFlow and ReynoldsFlow+ across three video-based benchmarks: tiny object detection on UAVDB, infrared object detection on Anti-UAV, and pose estimation on GolfDB. Experimental results demonstrate that networks trained with ReynoldsFlow+ achieve state-of-the-art (SOTA) performance, exhibiting improved robustness and efficiency across all tasks. The code is available at <https://github.com/wish44165/ReynoldsFlow>.

1. Introduction

Optical flow estimates pixel velocities by analyzing intensity changes between consecutive frames, playing a fundamental role in motion estimation [6, 20, 44, 47], object detection [1, 3, 4, 16, 38, 47], scene reconstruction [29, 47],

and video stabilization [22, 41, 45]. Historically, these applications have relied on traditional methods such as Horn-Schunck [8] and Lucas-Kanade [25], which are based on assumptions of local brightness constancy and spatial smoothness. However, these assumptions often break down in the presence of occlusions, fine-scale motion, or complex backgrounds. More recently, deep learning-based models, such as FlowNet [10] and FlowNet2 [17], have been proposed to learn optical flow. Additionally, some of these models directly integrate the learned optical flow into their architecture to warp images as an intermediate step for tasks like video frame interpolation. Although these models achieve impressive results, they typically require extensive training on synthetic datasets such as FlyingChairs and FlyingThings3D [10] and often struggle to generalize to real-world scenarios without further fine-tuning. In addition, the general approach to visualizing optical flow often uses HSV-based visualization, which aligns well with human perception by offering better discrimination power through Hue and Saturation. This makes it ideal for tasks such as color tuning, scene segmentation, and computer graphics, as highlighted in [24]. However, while HSV-based optical flow visualization enhances color saliency, it provides limited value for tasks where motion dynamics and structural variations are more critical than chromatic differences.

To preserve the training-free nature, we propose Reynolds flow, a novel optical flow framework grounded in the Reynolds transport theorem. By reinterpreting optical flow as a transport phenomenon of the light field associated with rigid motion, Reynolds flow models a broader range of transport phenomena, including complex motion dynamics and varying lighting conditions. In addition to the conventional HSV-based visualization, ReynoldsFlow, we introduce an enhanced representation, ReynoldsFlow+, which integrates optical flow magnitude, Reynolds flow magnitude, and frame intensity. This approach effectively distinguishes objects in videos with complex backgrounds and varying ambient lighting conditions, addressing the perceptual ambiguities caused by non-uniform color interpretation in HSV space. As demonstrated in Fig. 1, traditional HSV-

based optical flow fails to convey accurate motion features in challenging datasets [9, 18, 27], whereas ReynoldsFlow+ provides a more explicit perceptual representation of motion characteristics. Our contributions are as follows:

1. We propose Reynolds flow, a training-free optical flow estimation framework derived from the Reynolds transport theorem. We remove the brightness constancy assumption and generalize the traditional optical flow methods. This newly proposed flow is computationally efficient and robust for video-based tasks.
2. We introduce an enhanced visualization, ReynoldsFlow+, improving motion clarity for downstream tasks.
3. We perform comprehensive evaluations on real-world datasets, demonstrating SOTA accuracy in UAVDB and Anti-UAV for object detection and in GolfDB for pose estimation compared to the existing methods.

The rest of this paper is organized as follows: Sec. 2 reviews challenges in traditional and deep learning optical flow methods. Sec. 3 introduces Reynolds flow, ReynoldsFlow, and ReynoldsFlow+, detailing the theoretical foundations and innovations. Sec. 4 presents experimental results on three datasets and an in-depth analysis. Finally, Sec. 5 summarizes the paper and outlines future directions.

2. Related Work

2.1. Optical Flow Estimation Methods

Early optical flow methods like Horn-Schunck [15] and Lucas-Kanade [25] laid the foundation for optical flow estimation. Horn-Schunck applied global smoothness but struggled with large displacements and motion boundaries. At the same time, though computationally efficient, Lucas-Kanade was effective only for small, consistent motions and struggled in complex scenes. Later refinements, like Optimal Filter Estimation [35] and hybrid methods combining Lucas-Kanade and Horn-Schunck [8], aimed to balance adaptability and accuracy but still faced challenges with occlusion, noise, and textured backgrounds. Methods like Farneback’s polynomial expansion [12] and Brox’s high-accuracy flow estimation [7] focused on improving motion estimation but were computationally expensive. TV-L1 [46] addressed noise resilience, and SimpleFlow [39] offered a non-iterative solution at the cost of accuracy. RLOF [34] advanced feature tracking but still struggled with high-texture regions. Recent techniques aimed to balance accuracy with computational efficiency. DeepFlow [42] integrated deep matching for complex motions, while PCAFlow [43] reduced computational load. The Dense Inverse Search (DIS) algorithm [21] optimized dense flow estimation for time-sensitive applications. Despite these advancements, many methods still struggle with multiscale motion tracking and real-time processing, underscoring the need for improved robustness and efficiency in optical flow estimation.

The advent of deep learning has transformed optical flow estimation. FlowNet [10], the first CNN-based method, greatly improved motion recognition but struggled with fine-grained movements. FlowNet2 [17] enhanced precision with a cascaded architecture, while EpicFlow [32] integrated deep feature matching with variational refinement to improve boundary precision. PWC-Net [36] introduced a pyramid, warping, and cost-volume architecture that improved multiscale motion capture. Similarly, SpyNet [31] enhanced computational efficiency for real-time applications, and RAFT [40] set new benchmarks iteratively refining the flow field using contextual information. However, deep learning-based methods are limited by the need for retraining, posing challenges for deployment in resource-constrained environments like embedded systems.

2.2. Optical Flow in Video Processing

Optical flow estimation has been extensively studied in the context of standard benchmark datasets such as Sintel [2], KITTI [14], FlyingChairs, and FlyingThings3D [10]. While these datasets serve as valuable evaluation tools for assessing the accuracy of flow estimation methods, they primarily consist of synthetic or short video sequences designed for benchmarking rather than real-world applications. Much of the research focuses on optimizing pixel-wise flow accuracy, often treating optical flow as the end goal, as demonstrated by [10, 17, 32, 42, 43], rather than as a means of addressing practical computer vision challenges. Beyond benchmarking, optical flow has proven effective in practical applications such as video stabilization, where flow fields correct camera motion to produce smoother sequences [23], and frame interpolation, where flow-guided warping enhances temporal resolution for higher frame rates [13]. It also plays a crucial role in motion tracking, supporting object detection and activity recognition [30, 37]. However, optical flow images are typically treated as intermediate data within these frameworks, and the reason likely stems from traditional HSV-based visualizations, which fail to convey detailed texture information as presented in [5], even for large objects, thus restricting their practical application. A task similar to our UAV detection scenario is explored in [38], where a convolutional layer emulating the Lucas-Kanade optical flow is integrated into the YOLO architecture to enhance UAV detection. Similarly, [26] employs the Farneback optical flow method to track a player’s body posture and golf club trajectory, classifying them using multiple feature classification techniques. However, both approaches are ineffective due to the ambiguous visualization of optical flow images. To our knowledge, no existing method has demonstrated significant benefits in detecting moving objects and estimating poses by directly leveraging optical flow images in neural networks. This work investigates optical flow-based features, specifically Reynolds-

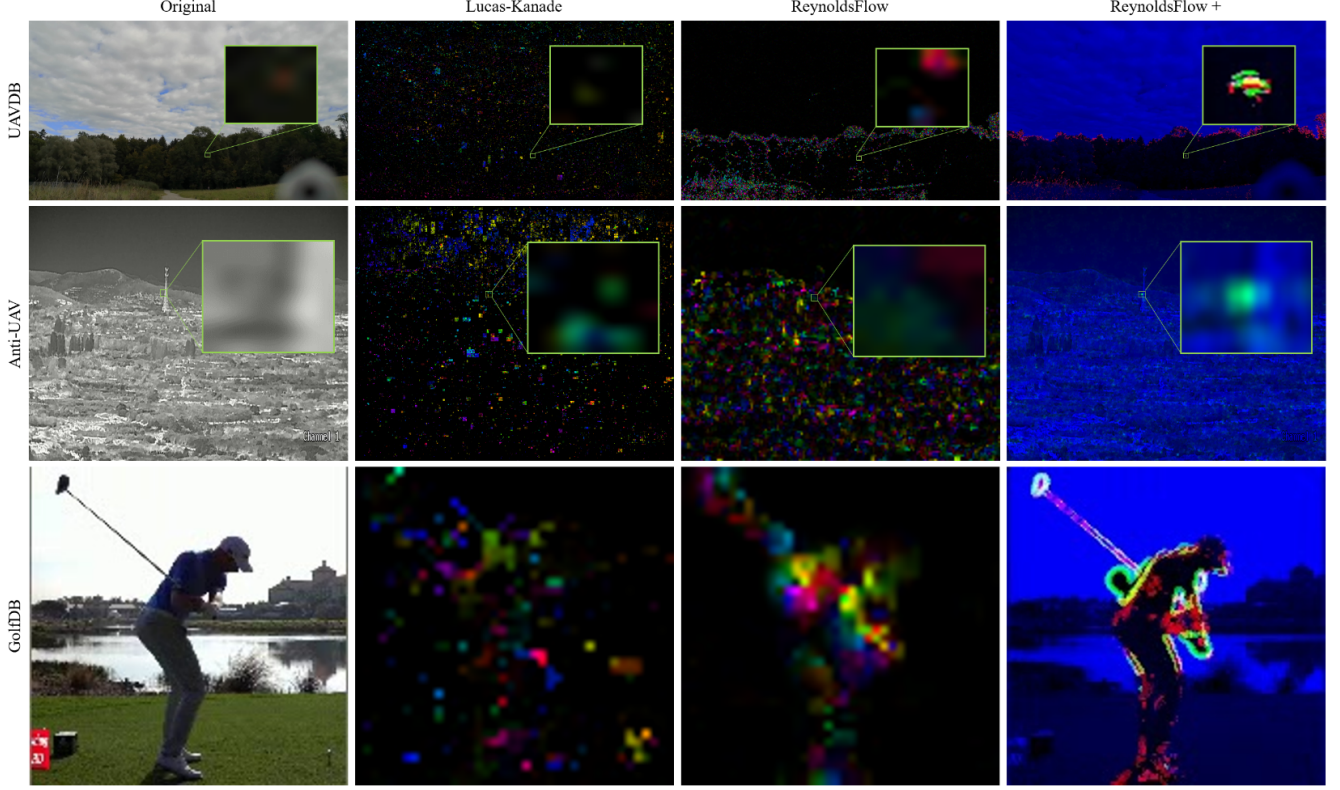


Figure 1. The first column shows original frames from UAVDB [9] (top), Anti-UAV [18] (middle), and GolfDB [27] (bottom). The second and third columns depict Lucas-Kanade optical flow and ReynoldsFlow, both visualized using the HSV color space. The last column presents the proposed ReynoldsFlow+ visualization, which enhances motion features in complex scenes.

Flow and ReynoldsFlow+, to analyze the impact on neural network performance in real-world scenarios.

3. Methodology

This section begins with the preliminaries, followed by the formulation of Reynolds flow, using the Reynolds transport theorem to provide a novel perspective on optical flow estimation. We then introduce an RGB-based visualization that enhances the clarity of motion features. Finally, we conduct a runtime analysis, comparing Reynolds flow with existing approaches to demonstrate its efficiency.

3.1. Preliminaries

3.1.1. Helmholtz decomposition

Let $\mathbf{v} \in C^1(\Omega, \mathbb{R}^2)$ be a continuously differentiable vector field defined on a domain Ω . According to the Helmholtz decomposition theorem, \mathbf{v} can be uniquely expressed as the sum of an irrotational (curl-free) component and a solenoidal (divergence-free) component:

$$\mathbf{v} = \mathbf{v}_r + \mathbf{v}_o, \quad (1)$$

where \mathbf{v}_r satisfies $\nabla \times \mathbf{v}_r = 0$ and \mathbf{v}_o satisfies $\nabla \cdot \mathbf{v}_o = 0$.

3.1.2. Reynolds transport theorem

Consider $f = f(\mathbf{p}, t)$ a smooth function where \mathbf{p} is defined on a time-dependent domain $\Omega(t)$. A grayscale video can be represented by $f(\mathbf{p}(t^n), t^n)$ where f is the intensity value at the pixel location $\mathbf{p}(t^n)$ in the view of field $\Omega(t^n)$ of the camera and t^n denotes the n th-frame image in the video footage. The Reynolds transport theorem shows that:

$$\begin{aligned} \frac{d}{dt} \int_{\Omega(t)} f dA &= \int_{\Omega(t)} \frac{\partial f}{\partial t} dA + \int_{\partial\Omega(t)} f(\mathbf{v} \cdot \mathbf{n}) dS \\ &= \int_{\Omega(t)} \frac{\partial f}{\partial t} dA + \int_{\Omega(t)} \nabla \cdot (f\mathbf{v}) dA \\ &= \int_{\Omega(t)} \left(\frac{\partial f}{\partial t} + \nabla f \cdot \mathbf{v} + f \nabla \cdot \mathbf{v} \right) dA. \end{aligned} \quad (2)$$

where $\mathbf{v} = \mathbf{v}(\mathbf{p}, t)$ is the velocity vector of \mathbf{p} at time t . For video footage, if the total intensity value remains constant and the velocity field \mathbf{v} is divergent-free for all time, then the Eq. (2) becomes

$$0 = \int_{\Omega(t)} \left(\frac{\partial f}{\partial t} + \nabla f \cdot \mathbf{v}_o \right) dA. \quad (3)$$

Assuming the integrand in the Eq. (3) equals zero, we obtain the brightness constancy constraint in the derivation of the traditional optical flows.

3.1.3. Area Jacobian in the domain transformation

Consider a region $\Omega(t)$ evolving over time t under the influence of a vector field \mathbf{v} . Let $\mathbf{p}^n = \begin{pmatrix} x^n \\ y^n \end{pmatrix} \in \Omega^n = \Omega(t^n)$

at time t^n , the corresponding vector field $\mathbf{v}^n = \begin{pmatrix} v_x^n \\ v_y^n \end{pmatrix}$ and time increment $\Delta t = t^{n+1} - t^n$ be uniform. Using the explicit Euler approximation, the domain transformation from Ω^n to Ω^{n+1} can be written as following:

$$\mathbf{p}^{n+1} \approx \mathbf{p}^n + \mathbf{v}^n(\mathbf{p}^n)\Delta t. \quad (4)$$

From Eq. (4), the differential wedge product $dx \wedge dy$ at \mathbf{p}^{n+1} can be approximated by the following:

$$\begin{aligned} dx^{n+1} \wedge dy^{n+1} &\approx (dx^n + dv_x^n \Delta t) \wedge (dy^n + dv_y^n \Delta t) \\ &= dx^n \wedge dy^n + dx^n \wedge dv_y^n \Delta t \\ &\quad + dv_x^n \Delta t \wedge dy^n + dv_x^n \Delta t \wedge dv_y^n \Delta t. \end{aligned}$$

Using the fact that $dv_x = \frac{\partial v_x}{\partial x} dx + \frac{\partial v_x}{\partial y} dy$ and $dv_y = \frac{\partial v_y}{\partial x} dx + \frac{\partial v_y}{\partial y} dy$, we have

$$dx^{n+1} \wedge dy^{n+1} = dx^n \wedge dy^n + \nabla \cdot \mathbf{v}^n dx^n \wedge dy^n \Delta t + \mathcal{O}((\Delta t)^2).$$

For sufficiently small Δt , this simplifies to:

$$dx^{n+1} \wedge dy^{n+1} \approx (1 + \nabla \cdot \mathbf{v}^n \Delta t) dx^n \wedge dy^n. \quad (5)$$

As a result, $(1 + \nabla \cdot \mathbf{v}^n \Delta t)$ is the approximal Jacobian between area differentials dA^n in Ω^n and dA^{n+1} in Ω^{n+1} . In other word, we have

$$dA^{n+1} \approx (1 + \nabla \cdot \mathbf{v}^n \Delta t) dA^n. \quad (6)$$

3.2. Derivation of Reynolds Flow

Let \mathbf{v}_o be the traditional optical flow that satisfies the constancy brightness assumption:

$$\frac{\partial f}{\partial t} + \nabla f \cdot \mathbf{v}_o = 0,$$

where \mathbf{v}_o is piecewise constant on on each window patch ω of the image. We have

$$\mathbf{v}_o^n = -(\nabla f)^\dagger \frac{\partial f}{\partial t}, \quad (7)$$

which forms the basis for classical optical flow methods, such as the Lucas-Kanade or Horn-Schunck approach. To extend optical flow estimation beyond traditional formulations, we consider a broader perspective based on the Reynolds transport theorem, which removes the brightness

constancy assumption and divergence-free restriction of the vector field \mathbf{v} . By Eq. (1), the Reynolds transport theorem can be reformulated as:

$$\frac{d}{dt} \int_{\Omega(t)} f dA = \int_{\Omega(t)} \left(\frac{\partial f}{\partial t} + \nabla f \cdot \mathbf{v}_o + \nabla f \cdot \mathbf{v}_r + f \nabla \cdot \mathbf{v}_r \right) dA. \quad (8)$$

By applying the Euler method on Eq. (8), the left-hand side (LHS) of the Eq. (8) satisfies

$$\begin{aligned} \text{LHS} &= \frac{1}{\Delta t} \left(\int_{\Omega^{n+1}} f^{n+1} dA^{n+1} - \int_{\Omega^n} f^n dA^n \right), \\ &\approx \frac{1}{\Delta t} \int_{\Omega^n} [(I + \nabla \cdot \mathbf{v}^n \Delta t) f^{n+1} - f^n] dA^n, \quad \text{by Eq. (6)} \\ &= \int_{\Omega^n} \left(\frac{f^{n+1} - f^n}{\Delta t} + f^{n+1} \nabla \cdot \mathbf{v}^n \right) dA^n. \end{aligned}$$

Next, applying the Taylor approximation

$$f^{n+1} - f^n \approx \frac{\partial f^n}{\partial t} \Delta t + \nabla f^n \cdot \begin{pmatrix} \Delta x^n \\ \Delta y^n \end{pmatrix},$$

and the Helmholtz decomposition of the vector field \mathbf{v} ,

$$\begin{aligned} \text{LHS} &\approx \int_{\Omega^n} \left(\frac{\partial f^n}{\partial t} + \nabla f^n \cdot \mathbf{v}^n + f^{n+1} \nabla \cdot \mathbf{v}^n \right) dA^n, \\ &= \int_{\Omega^n} \left(\frac{\partial f^n}{\partial t} + \nabla f^n \cdot (\mathbf{v}_r^n + \mathbf{v}_o^n) + f^{n+1} \nabla \cdot \mathbf{v}_r^n \right) dA^n. \end{aligned}$$

And the right hand (RHS) of Eq. (8) is simply as following

$$\text{RHS} = \int_{\Omega^n} \left(\frac{\partial f^n}{\partial t} + \nabla f^n \cdot (\mathbf{v}_r^n + \mathbf{v}_o^n) + f^n \nabla \cdot \mathbf{v}_r^n \right) dA^n,$$

By equating the LHS and the RHS above and setting $\delta f^n = f^{n+1} - f^n$, we obtain

$$\int_{\Omega^n} \delta f^n \nabla \cdot \mathbf{v}_r^n dA^n = 0.$$

The integration by part of the above equation leads to

$$\int_{\partial \Omega^n} \delta f^n \mathbf{v}_r^n \cdot \mathbf{n} dS^n - \int_{\Omega^n} \nabla \delta f^n \cdot \mathbf{v}_r^n dA^n = 0. \quad (9)$$

As usual, we can compute the vector field \mathbf{v}_r^n from Eq. (9) by assuming it remains constant within each local window patch ω . Specifically, we compute \mathbf{v}_r^n on a 3×3 window patch, denoted as $\omega_{3 \times 3}$. To approximate the boundary integral term in Eq. (9), we apply Simpson's rule:

$$\int_{\partial \omega_{3 \times 3}^n} \delta f^n \mathbf{v}_r^n \cdot \mathbf{n} dS^n \approx [\delta f_{b,x}^n, \delta f_{b,y}^n] \cdot \mathbf{v}_r^n, \quad (10)$$

here

$$(\delta f_b^n)_x = \frac{1}{3} \begin{bmatrix} 1 & 4 & 1 \\ 0 & 0 & 0 \\ -1 & -4 & -1 \end{bmatrix} * \delta f^n,$$

and

$$(\delta f_b^n)_y = \frac{1}{3} \begin{bmatrix} -1 & 0 & 1 \\ -4 & 0 & 4 \\ -1 & 0 & 1 \end{bmatrix} * \delta f^n.$$

The domain integral term in Eq. (9) is approximated as:

$$\begin{aligned} \int_{\omega^n} \nabla \delta f^n \cdot \mathbf{v}_r^n dA^n &= \int_{\omega^n} [(\nabla \delta f^n)_x, (\nabla \delta f^n)_y] \cdot \mathbf{v}_r^n dA^n \\ &\approx [(\nabla \delta f_\omega^n)_x, (\nabla \delta f_\omega^n)_y] \cdot \mathbf{v}_r^n, \end{aligned} \quad (11)$$

here

$$(\nabla \delta f_\omega^n)_x = \begin{bmatrix} 1 & 1 & 1 \\ 1 & 1 & 1 \\ 1 & 1 & 1 \end{bmatrix} * \left(\begin{bmatrix} -1 & 0 & 1 \\ -2 & 0 & 2 \\ -1 & 0 & 1 \end{bmatrix} * \delta f^n \right),$$

and

$$(\nabla \delta f_\omega^n)_y = \begin{bmatrix} 1 & 1 & 1 \\ 1 & 1 & 1 \\ 1 & 1 & 1 \end{bmatrix} * \left(\begin{bmatrix} -1 & -2 & -1 \\ 0 & 0 & 0 \\ 1 & 2 & 1 \end{bmatrix} * \delta f^n \right).$$

From Eq. (9), Eq. (10) and Eq. (11), we obtain the irrotational flow field:

$$\mathbf{v}_r^n = [(\delta f_b^n)_x - (\nabla \delta f_\omega^n)_x, (\delta f_b^n)_y - (\nabla \delta f_\omega^n)_y]^\perp.$$

Recall that the irrotational vector field \mathbf{v}_r^n complements the optical flow field \mathbf{v}_o^n derived from the Reynolds transport theorem. We refer to \mathbf{v}_r^n as the Reynolds flow. To ensure smoothness, we then define:

$$\mathbf{v}_r^n = \begin{bmatrix} G * (-(\delta f_b^n)_y + (\nabla \delta f_\omega^n)_y) \\ G * ((\delta f_b^n)_x - (\nabla \delta f_\omega^n)_x) \end{bmatrix}, \quad (12)$$

where G represents a Gaussian smoothing operator.

In the derivation of Reynolds flow, the optical flow component naturally cancels out from both sides of Eq. (9), allowing it to capture residual flow caused by lighting variations (e.g., shadows, infrared dimming) and non-rigid motion within the camera's field of view.

3.3. Flow Representation in Color Spaces

Optical flow visualization typically encodes motion magnitude and direction in HSV color space. The flow must be transformed back to RGB space to visualize it. This transformation is highly nonlinear and may lead to perceptual inconsistencies. Minor variations in hue and saturation may cause significant color shifts, making motion interpretation ambiguous. Moreover, accurate flow estimation remains challenging in scenes with mono textures, complex lighting, and dynamic motion. Tasks like moving object detection and motion analysis can become problematic due to non-uniform color variation when neural networks rely solely on HSV-based optical flow features. The robustness of neural networks can, therefore, deteriorate.

Here, we propose an alternative flow representation for Reynolds flow, denoted by ReynoldsFlow+, in which the traditional optical flow \mathbf{v}_o^n , the Reynolds flow \mathbf{v}_r^n , and the current frame intensity f^n are included. The **Reynolds-Flow**, \mathbf{v}_R^n , represents the combined flow field $\mathbf{v}_R^n = \mathbf{v}_r^n + \mathbf{v}_o^n$ encoded in the HSV space as in the traditional optical flow approach. On the other hand, the **ReynoldsFlow+**, \mathbf{v}_{R+}^n , denotes the introduced flow representation that stacks the magnitudes of the optical flow, Reynolds flow, and frame intensity together, i.e., $\mathbf{v}_{R+}^n = [|\mathbf{v}_o^n|, |\mathbf{v}_r^n|, f^n]_{rgb}$. Notice that the optical and Reynolds flow velocities' directional information is unneeded in the ReynoldsFlow+. Moreover, in the ReynoldsFlow+, the red and green channels capture the motion speed and the illuminant variations due to ambient lighting and motion, respectively; meanwhile, the spatial details of the current frame are preserved in the blue channel to enhance the contrast of the flow against the background. As shown in Fig. 1, ReynoldsFlow+ significantly improves the clarity of objects across all datasets.

3.4. Optical Flow Runtime Comparison

We present the runtime comparison of various optical flow algorithms on a system with an Intel Core i7-12650H CPU, NVIDIA RTX 4050 GPU, and 16 GB RAM. Specifically, we measure the average processing time per image on UAVDB using either CPU- or GPU-based implementations using OpenCV's publicly available packages. The GPU-accelerated methods, with the "cuda." prefix in the table, include Lucas-Kanade, Farneback, Brox, and TV-L1. Though a direct comparison across all methods is somewhat unfair, as they are not executed on the same processor type, we still select each method's fastest available OpenCV implementation to provide a realistic evaluation. For instance, we use the GPU-based Farneback method instead of its CPU counterpart due to its significantly higher efficiency. Similarly, other methods follow such selection criteria. The results in Tab. 1 demonstrate that ReynoldsFlow and ReynoldsFlow+ achieve the lowest computation times among CPU-based methods. In particular, ReynoldsFlow+ is slightly faster than ReynoldsFlow, eliminating the need for angle computation and HSV to RGB conversion. Consequently, ReynoldsFlow+ achieves the most efficient runtime and is almost comparable to the existing GPU-based approaches. Furthermore, our method is inherently adaptable to GPU acceleration, making ReynoldsFlow+ an efficient and practical choice for real-time applications.

4. Experimental Results

To evaluate the proposed ReynoldsFlow and ReynoldsFlow+, we conducted experiments on two tasks: 1) object detection on UAVDB [9] and Anti-UAV [18] and 2) pose estimation on GolfDB [27]. Compared against 12 approaches: 1) RGB videos, 2) grayscale videos and optical

Algorithms	OpenCV Packages	Runtime
Horn-Schunck [15]	–	1.951
Lucas-Kanade [25]	cuda_DensePyrLKOpticalFlow	0.013
Farneback [12]	cuda_FarnebackOpticalFlow	0.031
Brox [7]	cuda_BroxOpticalFlow	0.093
TV-L1 [46]	cuda_OpticalFlowDual_TVL1	3.165
SimpleFlow [39]	createOptFlow_SimpleFlow	3.302
RLOF [34]	createOptFlow_DenseRLOF	0.306
DeepFlow [42]	createOptFlow_DeepFlow	2.521
PCAFLOW [43]	createOptFlow_PCAFlow	0.403
DIS [21]	DISOpticalFlow_create	0.046
ReynoldsFlow	–	0.042
ReynoldsFlow+	–	0.041

Table 1. Runtime comparison (seconds) of optical flow algorithms on CPU or GPU for UAVDB per image.

flow methods, 3) Horn-Schunck, 4) dense Lucas-Kanade, 5) Farneback, 6) Brox, 7) TV-L1, 8) SimpleFlow, 9) RLOF, 10) DeepFlow, 11) PCAFlow, and 12) DIS. These methods were selected for their training-free nature, which aligns with our approach. All evaluations in Sec. 4 were performed on a high-performance computing system [28] with an NVIDIA H100 GPU with 80 GB memory.

4.1. Object Detection on UAVDB and Anti-UAV

We evaluate the proposed method in object detection tasks on two distinct datasets: UAVDB and Anti-UAV. UAVDB consists of high-resolution RGB frames (1920×1080 to 3840×2160) captured by a fixed camera, while Anti-UAV contains low-resolution infrared frames (512×512 to 640×512) captured by a moving camera. Both datasets feature single-class annotations and include multiple scales of UAVs, reflecting real-world scenarios where object sizes vary based on their distance from the camera. The UAVDB dataset includes 10,763 training images, 2,720 validation images, and 4,578 test images. Moreover, in the Anti-UAV dataset, we selected 4,800 training images, 1,600 validation images, and 1,600 test images from the 223 videos.

In the implementation details, we use YOLOv11n [19] as the detector, and all models were trained with eight workers, an input image size of 640×640, a batch size of 64, and over 100 epochs. Mosaic augmentation was applied throughout the training process, except during the last ten epochs, to stabilize performance. To leverage prior knowledge, we employed transfer learning by initializing the models with official YOLOv11n pre-trained weights and fine-tuning them on the UAVDB and Anti-UAV datasets. For evaluation, we report AP_{50} and AP_{50-95} metrics on the validation and test datasets. As shown in Tab. 2, YOLOv11n with ReynoldsFlow+ input achieves the highest performance in both datasets, demonstrating its effectiveness. Hereafter, we refer to this configuration using ReynoldsFlow+ input as YOLOv11nRF+.

4.2. Pose Estimation on GolfDB

We then evaluate the proposed method on the pose estimation task on GolfDB, which consists of 1,400 videos at a resolution of 160×160 pixels, with each video featuring subjects that occupy nearly the entire frame. The goal is to accurately identify specific poses within the golf swing sequence, which is divided into eight distinct events: Address (A), Toe-up (TU), Mid-backswing (MB), Top (T), Mid-downswing (MD), Impact (I), Mid-follow-through (MFT), and Finish (F). The dataset includes face-on and down-the-line views, offering diverse perspectives to capture the nuanced transitions between each event.

In the detailed implementation, we use SwingNet [27], a model designed for pose estimation in golf swing videos. We maintain the original training configuration, including a sequence length of 64, 10 frozen layers, a batch size of 22, 2,000 iterations, and six workers. We use the pre-trained MobileNetV2 model provided by [33] and then fine-tune it on the GolfDB dataset. Performance is evaluated using the Percentage of Correct Events (PCE) metric, with four-fold cross-validation to ensure reliability. For real-time videos sampled at 30 fps, a tolerance of $\delta = 1$ is used. For slow-motion videos, the tolerance is calculated as $\delta = \max(\lfloor \frac{N}{f} \rfloor, 1)$, where N is the number of frames from Address to Impact, f is the sampling frequency, and $\lfloor x \rfloor$ denotes rounding x to the nearest integer. As shown in Tab. 3, SwingNet with the ReynoldsFlow+ input achieves higher PCE than the other configurations. This configuration is referred to as SwingNetRF+.

4.3. Effectiveness of ReynoldsFlow+

To further assess the effectiveness of ReynoldsFlow+, we utilize HiResCAM [11] to visualize the activation maps learned by YOLOv11nRF+. The resulting heatmaps highlight regions of interest, revealing the model’s focus on key structures or objects. As shown in Fig. 2, the activation regions in YOLOv11nRF+ strongly align with the motion cues in ReynoldsFlow+ images for both UAVDB and Anti-UAV datasets. In contrast, the original YOLOv11n exhibits weak or inconsistent activation. These results suggest that ReynoldsFlow+ enhances the model’s ability to capture motion dynamics, reinforcing its significance for UAV detection. Furthermore, the findings highlight the critical role of input modalities in shaping the model’s decision-making process and provide deeper interpretability of motion analysis through HiResCAM. Heatmaps are unavailable for the GolfDB test since SwingNet employs a bidirectional LSTM for event probability prediction instead of relying on convolutional features. To evaluate the impact of ReynoldsFlow+, we analyze probability curves over time for each pose event. Fig. 3 (a) presents the keyframes of the eight events alongside their corresponding ReynoldsFlow+ images. In Fig. 3 (b), the solid and dashed lines denote the

Methods		UAVDB				Anti-UAV			
		AP_{50}^{val}	AP_{50-95}^{val}	AP_{50}^{test}	AP_{50-95}^{test}	AP_{50}^{val}	AP_{50-95}^{val}	AP_{50}^{test}	AP_{50-95}^{test}
YOLOv11n [19]	RGB	0.849	0.549	0.811	0.518	—			
	Grayscale / Infrared	0.770	0.338	0.660	0.281	0.785	0.424	0.781	0.418
	Horn-Schunck [15]	0.062	0.021	0.104	0.021	0.212	0.084	0.217	0.080
	Lucas-Kanade [25]	0.253	0.152	0.500	0.200	0.276	0.110	0.280	0.114
	Farneback [12]	0.465	0.264	0.258	0.145	0.476	0.235	0.500	0.246
	Brox [7]	0.454	0.218	0.244	0.110	0.396	0.172	0.388	0.168
	TV-L1 [46]	0.719	0.364	0.779	0.409	0.567	0.260	0.600	0.278
	SimpleFlow [39]	0.566	0.338	0.444	0.250	0.118	0.047	0.116	0.049
	RLOF [34]	0.172	0.079	0.097	0.039	0.477	0.212	0.472	0.222
	DeepFlow [42]	0.118	0.050	0.154	0.058	0.372	0.153	0.344	0.143
	PCAFLOW [43]	0.399	0.235	0.547	0.332	0.580	0.278	0.580	0.286
	DIS [21]	0.345	0.149	0.151	0.057	0.335	0.145	0.347	0.144
	ReynoldsFlow	0.500	0.325	0.500	0.288	0.643	0.313	0.646	0.320
	ReynoldsFlow+	0.910	0.571	0.895	0.547	0.812	0.465	0.792	0.446

Table 2. Comparison of YOLOv11n performance on UAVDB and Anti-UAV datasets with different input types.

	Methods	Average Loss	PCE
SwingNet [27]	RGB	0.2313	0.705
	Grayscale	0.2476	0.698
	Horn-Schunck [15]	0.2557	0.707
	Lucas-Kanade [25]	0.2268	0.692
	Farneback [12]	0.2545	0.717
	Brox [7]	0.2422	0.708
	TV-L1 [46]	0.1769	0.810
	SimpleFlow [39]	0.2775	0.665
	RLOF [34]	0.2562	0.668
	DeepFlow [42]	0.2142	0.716
	PCAFLOW [43]	0.1885	0.765
	DIS [21]	0.1995	0.772
	ReynoldsFlow	0.1763	0.804
	ReynoldsFlow+	0.1857	0.812

Table 3. Comparison of SwingNet performance on GolfDB dataset with different input types.

probability curves obtained using the original SwingNet and SwingNetRF+, respectively. Ground-truth event times are indicated by dashed vertical gray lines with corresponding event labels and the exact frame number. The results demonstrate that SwingNetRF+ consistently produces higher probability peaks across all events than the original SwingNet, significantly reducing prediction errors and uncertainty. Moreover, SwingNetRF+ achieves precise event frame predictions across all stages. These findings confirm that ReynoldsFlow+, by capturing motion dynamics, substantially enhances event detection accuracy in SwingNet.

Our experiments demonstrate that, except for ReynoldsFlow+, using optical flow images as input failed to outper-

form YOLOv11n with original video inputs on the UAVDB and Anti-UAV datasets. This suggests that directional motion features in traditional optical flow may be less crucial for UAV detection, as UAVs can move in arbitrary directions. In contrast, while some conventional optical flow methods using HSV-based visualization improved performance on GolfDB, where motion direction seems more intuitive and significant in pose estimation, ReynoldsFlow+ consistently outperformed these without relying on directional information. This is further supported by its more informative heatmaps and probability curves. Overall, ReynoldsFlow+ proves highly effective in detecting small objects and achieves the highest pose estimation accuracy.

5. Conclusion

This work proposes Reynolds flow, a training-free optical flow estimation framework grounded in the Reynolds transport theorem that generalizes traditional methods. Building on this framework, we introduce ReynoldsFlow and ReynoldsFlow+. We train YOLOv11n using these flow videos. Our experiments demonstrate that ReynoldsFlow+ provides more informative motion features even without the direction information of the flows. We evaluated these methods on diverse tasks, including object detection on UAVDB and Anti-UAV and pose estimation on GolfDB. ReynoldsFlow+ consistently improves accuracy on varying scales and complexities, serving as a practical preprocessing module that mitigates downstream learning difficulty without additional computational overhead. In addition, its high computational efficiency makes ReynoldsFlow+ ideal for real-time deployment on resource-constrained edge devices. Future work will explore the integration of ReynoldsFlow+ with learning-based systems on FPGAs to enhance scalability and versatility further.

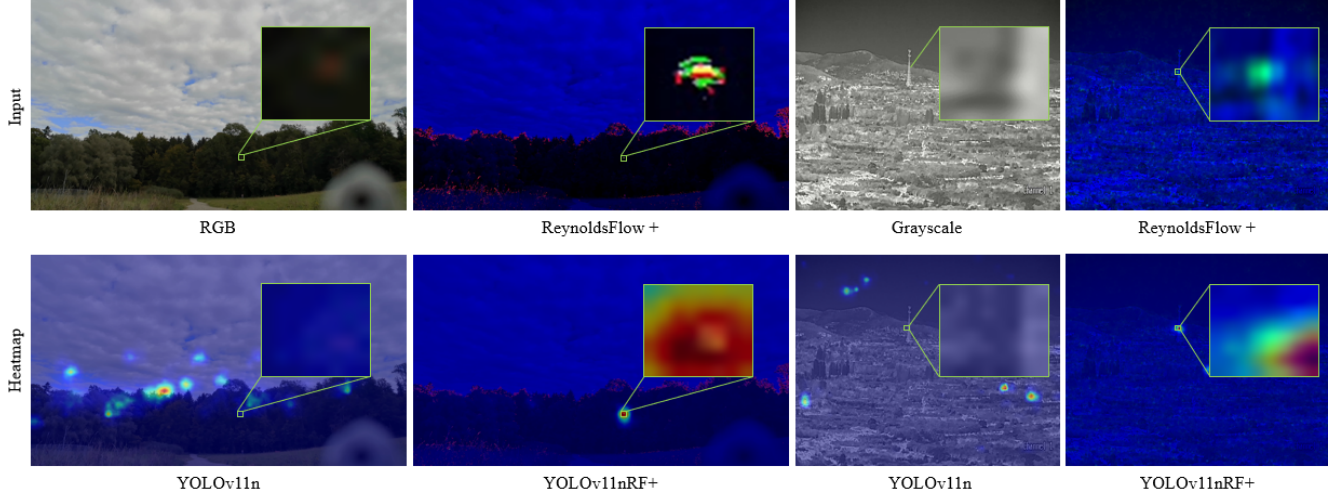


Figure 2. Visualization of inputs and HiResCAM heatmaps for UAVDB and Anti-UAV, with the UAV highlighted in the green box region.

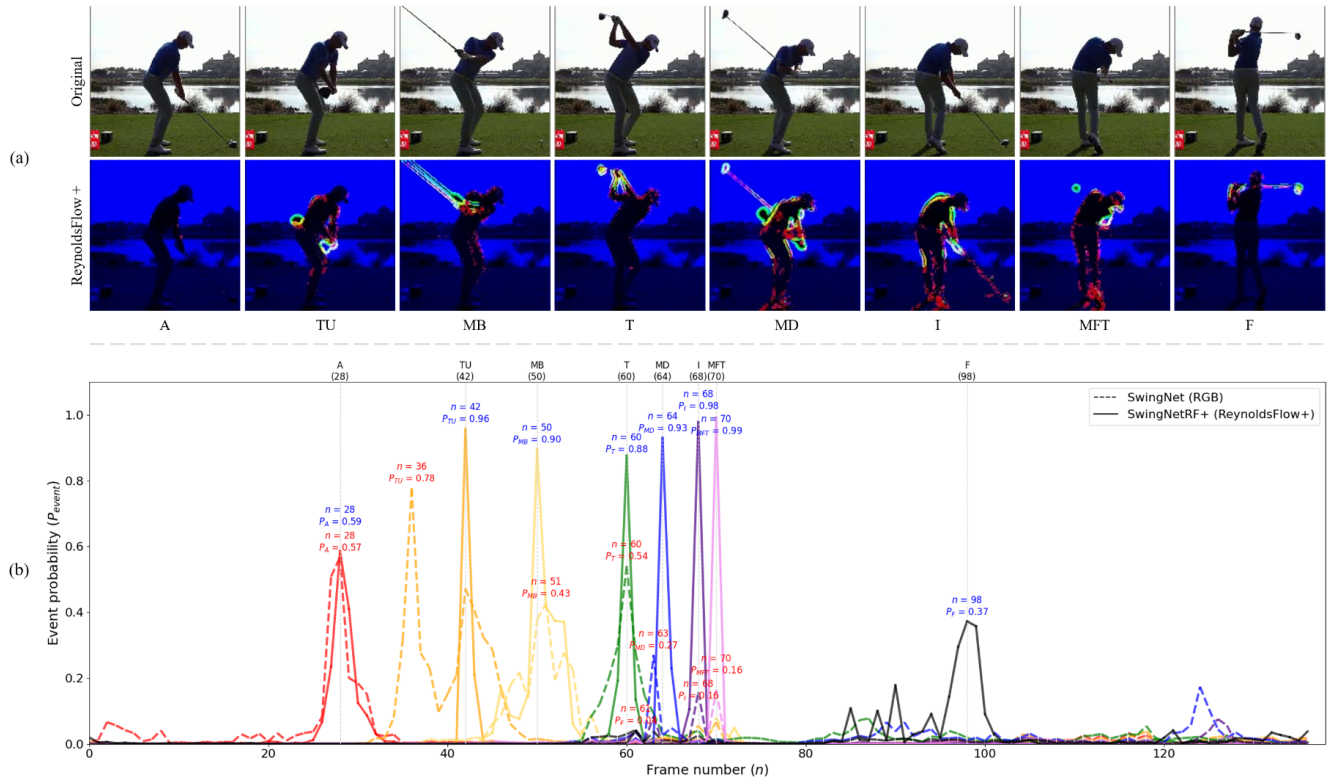


Figure 3. Comparison of event probabilities in a golf swing video clip using original video and ReynoldsFlow+ inputs. (a) Displays the eight key events with corresponding RGB frames and ReynoldsFlow+ visualizations. (b) Shows the probability curves for each event throughout the entire video. The x-axis represents the frame number (n), while the y-axis denotes the event probability (P_{event}). The predicted event frame is determined by selecting the frame with the highest probability.

References

- [1] Anshuman Agarwal, Shivam Gupta, and Dushyant Kumar Singh. Review of optical flow technique for moving object detection. In *2016 2nd international conference on contemporary computing and informatics (IC3I)*, pages 409–413. IEEE, 2016. 1
- [2] Sarah Alnegheimish, Dongyu Liu, Carles Sala, Laure Berti-Equille, and Kalyan Veeramachaneni. Sintel: A machine learning framework to extract insights from signals. In *Pro-*

- ceedings of the 2022 International Conference on Management of Data*, pages 1855–1865, 2022. 2
- [3] Yali Amit, Pedro Felzenszwalb, and Ross Girshick. Object detection. In *Computer Vision: A Reference Guide*, pages 875–883. Springer, 2021. 1
 - [4] Sepehr Aslani and Homayoun Mahdavi-Nasab. Optical flow based moving object detection and tracking for traffic surveillance. *International Journal of Electrical, Computer, Energetic, Electronic and Communication Engineering*, 7(9):1252–1256, 2013. 1
 - [5] Simon Baker, Daniel Scharstein, James P Lewis, Stefan Roth, Michael J Black, and Richard Szeliski. A database and evaluation methodology for optical flow. *International journal of computer vision*, 92:1–31, 2011. 2
 - [6] Thomas Brox and Jitendra Malik. Large displacement optical flow: descriptor matching in variational motion estimation. *IEEE transactions on pattern analysis and machine intelligence*, 33(3):500–513, 2010. 1
 - [7] Thomas Brox, Andrés Bruhn, Nils Papenberg, and Joachim Weickert. High accuracy optical flow estimation based on a theory for warping. In *Computer Vision-ECCV 2004: 8th European Conference on Computer Vision, Prague, Czech Republic, May 11-14, 2004. Proceedings, Part IV* 8, pages 25–36. Springer, 2004. 2, 6, 7
 - [8] Andrés Bruhn, Joachim Weickert, and Christoph Schnörr. Lucas/kanade meets horn/schunck: Combining local and global optic flow methods. *International journal of computer vision*, 61:211–231, 2005. 1, 2
 - [9] Yu-Hsi Chen. Uavdb: Trajectory-guided adaptable bounding boxes for uav detection. *arXiv preprint arXiv:2409.06490*, 2024. 2, 3, 5
 - [10] Alexey Dosovitskiy, Philipp Fischer, Eddy Ilg, Philip Hausser, Caner Hazirbas, Vladimir Golkov, Patrick Van Der Smagt, Daniel Cremers, and Thomas Brox. FlowNet: Learning optical flow with convolutional networks. In *Proceedings of the IEEE international conference on computer vision*, pages 2758–2766, 2015. 1, 2
 - [11] Rachel Lea Draelos and Lawrence Carin. Use hirescam instead of grad-cam for faithful explanations of convolutional neural networks. *arXiv preprint arXiv:2011.08891*, 2020. 6
 - [12] Gunnar Farneback. Two-frame motion estimation based on polynomial expansion. In *Image Analysis: 13th Scandinavian Conference, SCIA 2003 Halmstad, Sweden, June 29–July 2, 2003 Proceedings 13*, pages 363–370. Springer, 2003. 2, 6, 7
 - [13] Pedro Figueirêdo, Avinash Paliwal, and Nima Khademi Kalantari. Frame interpolation for dynamic scenes with implicit flow encoding. In *Proceedings of the IEEE/CVF winter conference on applications of computer vision*, pages 218–228, 2023. 2
 - [14] Andreas Geiger, Philip Lenz, Christoph Stiller, and Raquel Urtasun. Vision meets robotics: The kitti dataset. *The International Journal of Robotics Research*, 32(11):1231–1237, 2013. 2
 - [15] Berthold KP Horn and Brian G Schunck. Determining optical flow. *Artificial intelligence*, 17(1-3):185–203, 1981. 2, 6, 7
 - [16] Junjie Huang, Wei Zou, Jiagang Zhu, and Zheng Zhu. Optical flow based real-time moving object detection in unconstrained scenes. *arXiv preprint arXiv:1807.04890*, 2018. 1
 - [17] Eddy Ilg, Nikolaus Mayer, Tonmoy Saikia, Margret Keuper, Alexey Dosovitskiy, and Thomas Brox. FlowNet 2.0: Evolution of optical flow estimation with deep networks. In *Proceedings of the IEEE conference on computer vision and pattern recognition*, pages 2462–2470, 2017. 1, 2
 - [18] Nan Jiang, Kuiran Wang, Xiaoke Peng, Xuehui Yu, Qiang Wang, Junliang Xing, Guorong Li, Qixiang Ye, Jianbin Jiao, Zhenjun Han, et al. Anti-uav: a large-scale benchmark for vision-based uav tracking. *T-MM*, 2021. 2, 3, 5
 - [19] Glenn Jocher and Jing Qiu. Ultralytics yolo11, 2024. 6, 7
 - [20] Ibrahim Kajo, Aamir Saeed Malik, and Nidal Kamel. Motion estimation of crowd flow using optical flow techniques: A review. In *2015 9th International Conference on Signal Processing and Communication Systems (ICSPCS)*, pages 1–9. IEEE, 2015. 1
 - [21] Till Kroeger, Radu Timofte, Dengxin Dai, and Luc Van Gool. Fast optical flow using dense inverse search. In *Computer Vision-ECCV 2016: 14th European Conference, Amsterdam, The Netherlands, October 11–14, 2016. Proceedings, Part IV* 14, pages 471–488. Springer, 2016. 2, 6, 7
 - [22] Anli Lim, Bharath Ramesh, Yue Yang, Cheng Xiang, Zhi Gao, and Feng Lin. Real-time optical flow-based video stabilization for unmanned aerial vehicles. *Journal of Real-Time Image Processing*, 16:1975–1985, 2019. 1
 - [23] Shuaicheng Liu, Lu Yuan, Ping Tan, and Jian Sun. Steadyflow: Spatially smooth optical flow for video stabilization. In *Proceedings of the IEEE conference on computer vision and pattern recognition*, pages 4209–4216, 2014. 2
 - [24] Martin Loesdau, Sébastien Chabrier, and Alban Gabillon. Hue and saturation in the rgb color space. In *International conference on image and signal processing*, pages 203–212. Springer, 2014. 1
 - [25] Bruce D Lucas and Takeo Kanade. An iterative image registration technique with an application to stereo vision. In *IJCAI’81: 7th international joint conference on Artificial intelligence*, pages 674–679, 1981. 1, 2, 6, 7
 - [26] Jyoti Madake, Shreyas Sirshikar, Swagat Kulkarni, and Shripad Bhatlawande. Golf shot swing recognition using dense optical flow. In *2023 IEEE International Conference on Blockchain and Distributed Systems Security (ICBDS)*, pages 1–5. IEEE, 2023. 2
 - [27] William McNally, Kanav Vats, Tyler Pinto, Chris Dulhanty, John McPhee, and Alexander Wong. GolfdB: A video database for golf swing sequencing. In *Proceedings of the IEEE/CVF conference on computer vision and pattern recognition workshops*, pages 0–0, 2019. 2, 3, 5, 6, 7
 - [28] Bernard Meade, Lev Lafayette, Greg Sauter, and Daniel Tosello. Spartan hpc-cloud hybrid: delivering performance and flexibility. *University of Melbourne*, 10:49, 2017. 6
 - [29] Moritz Menze, Christian Heipke, and Andreas Geiger. Object scene flow. *ISPRS Journal of Photogrammetry and Remote Sensing*, 140:60–76, 2018. 1
 - [30] Manjunath Narayana, Allen Hanson, and Erik Learned-Miller. Coherent motion segmentation in moving camera

- videos using optical flow orientations. In *Proceedings of the IEEE international conference on computer vision*, pages 1577–1584, 2013. [2](#)
- [31] Anurag Ranjan and Michael J Black. Optical flow estimation using a spatial pyramid network. In *Proceedings of the IEEE conference on computer vision and pattern recognition*, pages 4161–4170, 2017. [2](#)
- [32] Jerome Revaud, Philippe Weinzaepfel, Zaid Harchaoui, and Cordelia Schmid. Epicflow: Edge-preserving interpolation of correspondences for optical flow. In *Proceedings of the IEEE conference on computer vision and pattern recognition*, pages 1164–1172, 2015. [2](#)
- [33] Mark Sandler, Andrew Howard, Menglong Zhu, Andrey Zhmoginov, and Liang-Chieh Chen. Mobilenetv2: Inverted residuals and linear bottlenecks. In *Proceedings of the IEEE conference on computer vision and pattern recognition*, pages 4510–4520, 2018. [6](#)
- [34] Tobias Senst, Volker Eiselein, and Thomas Sikora. Robust local optical flow for feature tracking. *IEEE Transactions on Circuits and Systems for Video Technology*, 22(9):1377–1387, 2012. [2, 6, 7](#)
- [35] Nusrat Sharmin and Remus Brad. Optimal filter estimation for lucas-kanade optical flow. *Sensors*, 12(9):12694–12709, 2012. [2](#)
- [36] Deqing Sun, Xiaodong Yang, Ming-Yu Liu, and Jan Kautz. Pwc-net: Cnns for optical flow using pyramid, warping, and cost volume. In *Proceedings of the IEEE conference on computer vision and pattern recognition*, pages 8934–8943, 2018. [2](#)
- [37] Shuyang Sun, Zhanghui Kuang, Lu Sheng, Wanli Ouyang, and Wei Zhang. Optical flow guided feature: A fast and robust motion representation for video action recognition. In *Proceedings of the IEEE conference on computer vision and pattern recognition*, pages 1390–1399, 2018. [2](#)
- [38] Yu Sun, Xiyang Zhi, Haowen Han, Shikai Jiang, Tianjun Shi, Jinnan Gong, and Wei Zhang. Enhancing uav detection in surveillance camera videos through spatiotemporal information and optical flow. *Sensors*, 23(13):6037, 2023. [1, 2](#)
- [39] Michael Tao, Jiamin Bai, Pushmeet Kohli, and Sylvain Paris. Simpleflow: A non-iterative, sublinear optical flow algorithm. In *Computer graphics forum*, pages 345–353. Wiley Online Library, 2012. [2, 6, 7](#)
- [40] Zachary Teed and Jia Deng. Raft: Recurrent all-pairs field transforms for optical flow. In *Computer Vision–ECCV 2020: 16th European Conference, Glasgow, UK, August 23–28, 2020, Proceedings, Part II 16*, pages 402–419. Springer, 2020. [2](#)
- [41] Yiming Wang, Qian Huang, Chuanxu Jiang, Jiwen Liu, Mingzhou Shang, and Zhuang Miao. Video stabilization: A comprehensive survey. *Neurocomputing*, 516:205–230, 2023. [1](#)
- [42] Philippe Weinzaepfel, Jerome Revaud, Zaid Harchaoui, and Cordelia Schmid. Deepflow: Large displacement optical flow with deep matching. In *Proceedings of the IEEE international conference on computer vision*, pages 1385–1392, 2013. [2, 6, 7](#)
- [43] Jonas Wulff and Michael J Black. Efficient sparse-to-dense optical flow estimation using a learned basis and layers. In *Proceedings of the IEEE Conference on Computer Vision and Pattern Recognition*, pages 120–130, 2015. [2, 6, 7](#)
- [44] Li Xu, Jiaya Jia, and Yasuyuki Matsushita. Motion detail preserving optical flow estimation. *IEEE Transactions on Pattern Analysis and Machine Intelligence*, 34(9):1744–1757, 2011. [1](#)
- [45] Jiyang Yu and Ravi Ramamoorthi. Learning video stabilization using optical flow. In *Proceedings of the IEEE/CVF conference on computer vision and pattern recognition*, pages 8159–8167, 2020. [1](#)
- [46] Christopher Zach, Thomas Pock, and Horst Bischof. A duality based approach for realtime tv-l 1 optical flow. In *Pattern Recognition: 29th DAGM Symposium, Heidelberg, Germany, September 12-14, 2007. Proceedings 29*, pages 214–223. Springer, 2007. [2, 6, 7](#)
- [47] Mingliang Zhai, Xuezhi Xiang, Ning Lv, and Xiangdong Kong. Optical flow and scene flow estimation: A survey. *Pattern Recognition*, 114:107861, 2021. [1](#)